HHS Public Access

Author manuscript

Nat Med. Author manuscript; available in PMC 2015 November 01.

Published in final edited form as:

Nat Med. 2015 May ; 21(5): 476–482. doi:10.1038/nm.3851.

Photovoltaic restoration of sight with high visual acuity

Henri Lorach[1,2,3,†], **Georges Goetz**[1,4,*,†], **Richard Smith**[5], **Xin Lei**[4], **Yossi Mandel**[6], **Theodore Kamins**[4], **Keith Mathieson**[7], **Philip Huie**[1,2], **James Harris**[4], **Alexander Sher**[5,‡], and **Daniel Palanker**[1,2,‡]

[1]Hansen Experimental Physics Laboratory, Stanford University, Stanford, CA, USA

[2]Department of Ophthalmology, Stanford University, Stanford, CA, USA

[3]Inserm UMR_S968, Institut de la Vision, Paris, France

[4]Department of Electrical Engineering, Stanford University, Stanford, CA, USA

[5]Santa Cruz Institute for Particle Physics, University of California Santa Cruz, Santa Cruz, CA, USA

[6]The Mina & Everard Goodman Faculty of Life Sciences, Bar Ilan University, Israel

[7]Institute of Photonics, University of Strathclyde, Glasgow, UK

Abstract

Patients with retinal degeneration lose sight due to gradual demise of photoreceptors. Electrical stimulation of the surviving retinal neurons provides an alternative route for delivery of visual information. We demonstrate that subretinal arrays with 70 μm photovoltaic pixels provide highly localized stimulation, with electrical and visual receptive fields of comparable sizes in rat retinal ganglion cells. Similarly to normal vision, retinal response to prosthetic stimulation exhibits flicker fusion at high frequencies, adaptation to static images and non-linear spatial summation. In rats with retinal degeneration, these photovoltaic arrays provide spatial resolution of 64 ± 11 μm, corresponding to half of the normal visual acuity in pigmented rats. Ease of implantation of these wireless and modular arrays, combined with their high resolution opens the door to functional restoration of sight.

*Correspondence to: ggoetz@stanford.edu.
†These authors contributed equally to this work, and share primary authorship.
‡These authors contributed equally to supervision of this work, and share senior authorship.

Author contributions

X.L. fabricated the subretinal implants under the supervision of T.K., K.M., J.H. and D.P.. G.G., R.S., D.P. and A.S. designed the in-vitro experiments. R.S. and G.G. performed the in-vitro experiments. H.L., D.P. and Y.M. designed the in-vivo experiments. H.L., Y.M. and P.H. performed the in-vivo experiments. G.G. and H.L. analyzed the data. G.G., H.L., A.S. and D.P. wrote the paper.

Financial disclosure

D.P.'s patents related to retinal prosthesis are owned by Stanford University and licensed to Pixium Vision.
D.P. is a consultant for Pixium Vision.

Introduction

Retinal degenerative diseases such as age-related macular degeneration and retinitis pigmentosa lead to blindness due to gradual loss of photoreceptors, while the inner retinal neurons survive to a large extent[1,2], albeit with some rewiring[3,4]. Retinal prostheses aim at restoring sight by electrical stimulation of these surviving neurons. In the epiretinal approach, the primary targets of stimulation are the retinal ganglion cells (RGCs)[5,6], while subretinal stimulation elicits visual responses via inner retinal neurons (primarily bipolar cells)[7–9]. Both approaches were recently approved for clinical use, but these systems involve bulky implanted electronics with trans-scleral cables and require very complex surgeries. In addition, visual acuity with the epiretinal system (ARGUS II, Second Sight Inc., USA) is no better than 20/1260[6], and the percepts are distorted due to axonal stimulation[10]. Subretinal prostheses (Alpha IMS, Retina Implant AG, Germany) provided similar acuity levels, mostly below 20/1000 except for one patient who reached 20/550[11].

We developed an alternative approach to retinal prosthetics, in which photovoltaic subretinal pixels convert pulsed light into electric current and are therefore completely wireless[12,13]. Bright pulsed illumination is provided by image projection from video goggles and avoids photophobic effects by using near-infrared (NIR, 880 – 915nm) light. Pulsed illumination is necessary to provide charge-balanced stimulation, which is critical for electrochemical biocompatibility in chronic use. Optical delivery of the visual information preserves the natural link between ocular movement and image perception, unlike systems where the electrodes are connected to an external camera via serial telemetry. Photovoltaic arrays with three diodes per pixel can safely elicit and modulate retinal responses, both in-vitro and in-vivo, in normally sighted (Long Evans or Wild Type, WT) and in blind (Royal College of Surgeons, RCS) rats[12,14,15].

In this study, we evaluate spatio-temporal characteristics of prosthetic vision, including one of its most important properties: the spatial resolution of the retinal response in-vitro and visual acuity in-vivo.

Results

Electrical receptive fields

The prosthetic devices used throughout the study consisted of a hexagonal array of 70 μm pixels separated by 5 μm trenches, corresponding to a 65 μm pitch between adjacent rows (Fig. 1a–b). Pixels consisted of several photodiodes connected in series, delivering anodic-first charge-balanced pulses of current. Individual return electrodes were incorporated into each pixel to localize the stimulation current. A resistance between the active and return electrodes acted like a shunt resistor and helps discharge the electrodes between the pulses (Fig. 1c).

We conducted *in-vitro* evaluation of the spatial resolution of the retinal response to photovoltaic stimulation and to visible light by recording from hundreds of retinal ganglion cells (RGCs) in the rat retina using a large-scale multi-electrode array system[16] (Fig. 1d, Supplementary Fig. 1). In a normal retina, visual information transduced by the

photoreceptors is further processed in the inner nuclear layer before it is transmitted to the ganglion cells. The visual receptive fields (vRFs) of different ganglion cell types form complementary mosaics over the retinal surface[17–20], and define the characteristics of retinal processing. Here, we compare these vRFs (Fig. 2a) obtained with a spatio-temporal binary white noise stimulus[21] to the response properties with electrical stimulation. We mapped the electrical receptive fields (eRFs) of the RGCs (Fig. 2b, d) using a sparse NIR binary noise stimulus projected onto the photovoltaic pixels (Supplementary Fig. 2 and Methods). Gray levels encode the average number of network-mediated action potentials elicited in the RGC. The stimulation artifact caused by the implant on multi-electrode array prevented detection of possible short-latency action potentials resulting from direct stimulation of ganglion cells. However, the stimulation parameters we used in this study were shown to selectively elicit network-mediated responses[14,22,23]. The response latencies we observed with photovoltaic activation were consistent with stimulation originating at the photoreceptor terminals or in the inner nuclear layer. Previous studies demonstrated that blocking all synaptic connections eliminated RGC responses, while blocking the transmission between photoreceptors and ON-bipolar cells did not affect the response from ON RGCs, confirming that the stimulation occurs at the bipolar cell level[12].

The average eRF diameter was 248 ± 59 μm in WT and 203 ± 63 μm in degenerate RCS retinas (Fig. 2d). With visible light, the average diameter of the WT vRFs was 244 ± 32 μm (Fig. 2d), not substantially different from the eRF sizes. Despite recording from a wide variety of RGCs in WT retina (ON and OFF, transient and sustained, brisk and sluggish cells[24]) with a variety of RF diameters, we did not observe any correlation between eRF and vRF sizes.

Some eRFs in both the WT and RCS retinas (16 out of 140 neurons) had a more complex structure, displaying a localized and a diffuse, “donut-shaped” component. Both of them exhibited excitatory response, but with different latencies (Fig. 2c, Supplementary Fig. 3). These eRFs with a diffuse component were not included in the eRF average size (Fig. 2d, triangles).

Retinal response to grating contrast reversal

While measuring the spatial extent of electrical receptive fields obtained with a sparse white noise provides an indication of achievable spatial resolution, it does not take into account possible non-linear effects of presenting more complex stimuli. In order to account for this, we characterized retinal responses to alternating square gratings of various spatial frequencies using visible light and photovoltaic stimulation (see Methods). This type of stimulus is routinely used for measuring visual acuity in-vivo[25–27]. Experiments were conducted with RCS retinas for photovoltaic stimulation (4 ms pulses, 5 mW/mm^2 irradiance NIR pulses) and with WT retinas for visible-light stimulation (10 ms, 591 nm pulses, low photopic regime) and the width of the square-wave grating stripes varied from 7 to 300 μm. Visible and NIR images were projected with 20 Hz flicker frequency and 1 Hz grating alternation. Photovoltaic stimulation requires pulsed illumination to provide charge-balanced pulses of electric current, and we performed visible-light stimulation in the same way for better comparison.

Electrical stimulation of the RCS retina resulted in a continuum of responses, ranging from a combination of strong transient responses to the alternating grating with very weak response to individual pulses at 20 Hz (flicker-fused), to more robust responses to every stimulation pulse (Fig 4c). In the WT retina we observed very little, if any response to individual pulses of visible light at 20 Hz, and strong responses to the grating reversal (Fig 4b). Thus a substantial fraction (about half) of the RCS rat RGCs under electrical stimulation and virtually all WT rat RGCs under visual stimulation responded to the grating contrast reversal and not to every pulse of light (Fig. 3a, Fig. 4b–c), illustrating the flicker fusion and adaptation to static images phenomena.

To assess the spatial resolution of the retinal response to photovoltaic and visible-light stimulation, we quantified the strength of the RGC response to grating contrast reversal as a function of the stripe width (see Methods). This response, measured in action potentials elicited per grating reversal, decreased with increasing spatial frequency of the gratings, both for visible-light and electrical stimulation (Fig. 3b).

We defined stimulation threshold as the grating stripe size that resulted in a 50% probability of eliciting an action potential correlated with the grating contrast reversal (see Methods). The distribution of thresholds measured with visible-light stimulation peaked at a stripe width of 28 μm in one of the preparations and at a stripe width of 48 μm in the other (Supplementary Fig. 4). The difference is most likely due to differences in eccentricity of the retinal sections we recorded from. With photovoltaic stimulation, the distribution exhibited a peak at 67 μm per stripe, with a large tail extending to widths greater than 100 μm (Fig. 3c, 109 RGCs, $n = 4$ preparations).

Responses of the neurons to gratings smaller than their receptive field diameter, whether electrical or visible, can be explained by non-linear interactions in receptive field subunits[24,28,29]. For visible light, the peak corresponds to neurons responding to each phase of the grating alternation (Fig. 3a, Fig. 4b). This classical frequency doubling of the response is indicative of nonlinear spatial summation[24,29]. Similarly, neurons responded to gratings with 67 μm stripe width in NIR with frequency doubling (Fig. 3a, Fig. 4c), demonstrating non-linear summation inside the RGC electrical receptive fields with the size of the effective non-linear subunits comparable to our pixel pitch (Fig. 1a). 71% of RCS neurons that responded to grating stipe widths smaller than 75 μm exhibited frequency doubling in their responses (min/max ratio of the peak of the response to each phase of the grating exceeding 0.75), consistent with non-linear summation in receptive field subunits. All neurons that exhibited complete flicker fusion with photovoltaic stimulation (i.e., no response to 20 Hz pulses without the change of the projected image) responded to gratings contrast reversal with stripe widths smaller than 100 μm.

Subretinal implantations in-vivo

For in-vivo testing of prosthetic vision we implanted the photovoltaic arrays subretinally in 16 rats ($n = 9$ WT, $n = 7$ RCS). Fluorescein angiography confirmed normal retinal blood perfusion above the implant (Fig. 5a). Optical coherence tomography (OCT) performed one week after surgery demonstrated close and stable proximity of the inner nuclear layer to the implant (Fig. 5b).

In WT rats, presence of the subretinal implant caused degeneration of the photoreceptors above the chip, while the inner nuclear layer (INL) and ganglion cell layer (GCL) were well-preserved[14]. This local outer retinal degeneration is likely due to separation of the photoreceptor outer segments from the retinal pigment epithelium and isolation from choroidal perfusion.

Cortical response thresholds and dynamic range

We assessed response of the visual system by recording visually evoked potentials (VEPs) induced either by the implant activated with pulsed NIR light (eVEP), or by visible light projected onto normal retina (Fig. 5c and Methods). We used a camera mounted on a slit lamp to visualize the stimulus on the retina and control the position of the beam relative to the implant.

Photovoltaic stimulation thresholds (see Methods, [14]) did not differ substantially between WT and RCS rats. With 10 ms pulses and 2 Hz repetition rate, the stimulation thresholds were 0.55 ± 0.08 mW/mm^2. Amplitude of the eVEP increased with irradiance between 0.125 mW/mm^2 and 1 mW/mm^2, saturating at higher light intensity (Fig. 6a). Increasing pulse duration from 1 ms to 10 ms also increased cortical response, which saturated at longer pulse durations (Fig. 6b). Therefore, cortical response to photovoltaic subretinal stimulation can be modulated either by irradiance or pulse duration over an order of magnitude-wide dynamic range.

Visual acuity

One of the established methods for assessing visual acuity in animals and in human infants is based on cortical response to alternating gratings of various spatial frequencies, recorded through visually evoked potentials (VEPs)[25,26]. This method matches well the visual acuity measured in behavioral tests[27,30].

We recorded the cortical responses to such alternating NIR patterns in implanted RCS rats (Fig. 6c) and to the same patterns presented with visible light in WT animals on healthy retina outside the implanted area. The square-wave grating patterns were projected using 4 ms pulses at 40 Hz repetition rate and reversing the contrast at 1 Hz. Grating stripe width varied from 6 μm to 200 μm. The VEP amplitude decreased with increasing spatial frequency for both visible and electrical stimulation (Fig. 6d).

With electrical stimulation, 100 μm stripes elicited robust responses in all RCS rats and eVEP amplitudes were significantly different from noise level ($P < 0.01$, one-tailed Welch t-test). With 75 μm gratings the signal amplitude was still above the noise level (by 29%), but the difference was not statistically significant ($P = 0.097$). In WT animals, responses to visible-light stripes of 50 μm width were significantly above the noise level ($P < 0.05$), but gratings with 25 μm stripes did not elicit significant responses ($P = 0.17$) (Fig. 6d).

We estimated the acuity limit by extrapolating the measured data down to the noise level (Fig. 6d and Methods). For prosthetic vision in RCS rats, the limit and corresponding uncertainty (see Methods) was 64 ± 11 μm per stripe, as compared to 27 ± 9 μm per stripe in WT animals stimulated with visible light. These results correspond to 0.47 and 1.1 cycle per

degree (cpd), respectively, in close agreement with the 1 to 1.2 cpd visual acuity of pigmented rats reported in the literature[25–27,30].

To confirm that these responses were conveying spatial information rather than charge accumulation or an illumination misbalance between the two phases of the grating, we recorded the stimuli on the cornea and reproduced similar transitions with a full-field stimulus devoid of spatial content (Supplementary Fig. 5). For all grating sizes, the equivalent spatially uniform stimulus did not trigger any detectable VEP response (< 6 times noise variance), thus confirming that the grating response did involve spatial modulation. Additionally, RCS rats did not respond to alternating gratings projected onto the implanted area with visible light, and did not respond to pulsed infrared light projected away from the implant either (Supplementary Fig. 6).

Discussion

Pixels of the current photovoltaic implants were redesigned based on a recent optimization of the subretinal stimulation protocols[23], so as to deliver anodic-first pulses of current. The resulting cortical activation threshold in WT and RCS rats implanted with 70 μm pixel arrays was 0.55 mW/mm^2 with 10 ms pulses – four times lower than the threshold previously reported by our group with implants delivering cathodic-first pulses[12,14], and more than two orders of magnitude below the ocular safety limit for the 880–915 nm wavelength range (Methods, [31,32]). Low stimulation thresholds are important for the development of compact, safe and efficient video goggles activating the implants in human subjects[33], and also indicate that pixel size could be reduced further by about a factor of 2, thereby enabling higher spatial resolution. However, stimulation thresholds likely depend on the characteristics of the retinal network and extent of degeneration. At the highest settings used in this study, stimulation for many hours at a time in-vitro and in-vivo did not decrease responsiveness or produce any signs of tissue damage, confirming safety of the NIR irradiation settings. While the results with rats are certainly encouraging, further testing in larger animals will be required to assess safety and efficacy of stimulation prior to human use.

Similarity of the stimulation thresholds between WT and RCS rats in-vivo is likely due to local degeneration of the photoreceptors above the implants[14]. In WT animals, the chronic separation of photoreceptors from the RPE caused by the implant triggers a progressive loss of photoreceptors. A few weeks after implantation, in both animal models, the outer retina has degenerated and bipolar cells achieved similar proximity to the electrodes.

In natural vision, the retina acts as a temporal band-pass filter transmitting local changes in luminance within a certain range of temporal frequencies. The low end of this frequency band represents the effect of fading of static images, which typically occurs within seconds, for example when eye movements are disabled[34]. The high end of this band corresponds to flicker fusion (image fusion) at high frequencies, resulting in a continuous perception of movies with a frame rate exceeding 20 Hz. A similar effect of flicker fusion was observed with network-mediated electrical stimulation of the retina and has previously been referred to as “desensitization” [8]. This desensitization results in fading of a static image transferred to

the retina with high frequency stimulus and was therefore considered detrimental for vision restoration. However, we argue that our results in-vitro and in-vivo demonstrate it can be interpreted as flicker fusion and adaptation to static images, a natural feature of vision. With high flicker frequency in our experiments (20 – 40 Hz), the retina responded primarily to luminance transitions of the image rather than individual pulses of light. Therefore, the network-mediated retinal response to electrical stimulation appears to preserve these three features of normal vision: (1) fusion of high frequency flicker, (2) adaptation to static images, and (3) response to image changes at lower frequencies, similar to the natural "event-based" language of the retina[35].

One of the most important characteristics of vision in general and prosthetic restoration of sight in particular, is visual acuity. Both the epiretinal and subretinal implants tested in clinical trials enabled rather low acuity, which varied greatly among the patients. The majority of patients could not read and among the few who could, visual acuity was mostly below 20/1200, except for a single patient who was reported to achieve 20/550[11]. Local return electrodes in our photovoltaic pixels provide much tighter confinement of electric field compared to monopolar electrodes in other implants. This helps reduce cross-talk between neighboring electrodes, thereby increasing contrast and spatial resolution of the stimulation[36,37].

Photovoltaic pixels elicited highly localized responses in both normal and degenerate retinas, with electrical receptive fields of individual RGCs in the RCS retina having a size similar to those of the visually evoked receptive fields in the WT retina. A minority of RGCs (16 out of 140) responded with an additional diffuse component involving mechanisms that remain to be explored. However, since RGCs responded to alternating gratings down to 28 μm/stripe with visible light, and to 67 μm/stripe with photovoltaic stimulation, it appears that the resolution-limiting factor is the pixel size and its reduction might further improve localization of the retinal response.

Measurements of cortical and retinal responses to alternating gratings demonstrated that, similarly to normal vision, a degenerate retina stimulated via the prosthetic device could extract features smaller than the RGC receptive fields. This non-linear summation of subunits within the ganglion cell receptive fields[38–42] is another important function of the retinal neural network utilized with a subretinal prosthesis. More generally, retinal response to prosthetic stimulation with stripe widths similar to the pixel spacing demonstrates excellent localization of the stimulus over the 70 μm pixels, without much interference from neighboring electrodes for this relatively complex stimulus.

Extrapolating from the measured sizes of electrical receptive fields and their non-linear subunits to expected perceptual acuity in human subjects is difficult because it is yet unclear whether high acuity vision in rats is mediated by midget-like retinal ganglion cells with small receptive fields – as appears to be the case in primates[43] – or whether population effects are responsible for it. To provide single-pixel resolution for central vision in humans, midget cells in the fovea (within 2.5 degrees of eccentricity) would have to respond to stimulation from a single pixel only. Because of our limited ability to record from cells with very small receptive fields in the rat retina, we could not show directly that small ganglion

cells can be stimulated in such a spatially selective fashion. Our results are likely to be applicable to more peripheral regions of the primate retina where ensemble responses of ganglion cells might play a role in improving spatial resolution beyond their individual receptive field sizes. Within a few months of retinal degeneration in rats, the size of electrical receptive fields did not increase compared to the healthy retina. However, it remains to be seen whether retinal rewiring at more advanced stages of degeneration in human subjects will affect the spatial confinement of the stimulation and its thresholds.

Spatial frequency cutoff measured in-vivo was similar to the results in-vitro, but it was easier to interpret in terms of perceptual visual acuity restored in the rat[25,26]. Extrapolation of the measured data down to the noise level yielded an estimate of the acuity limit of 64 ± 11 μm/stripe or 0.47 cpd for prosthetic stimulation, matching the pixel row pitch of the implant (65 μm). This is only twice below the normal vision in rats: 27 ± 9 μm/stripe or 1.1 cpd. The human eye is approximately 5 times larger than the rat eye, and a resolution of 64μm per stripe on a human retina corresponds to 2.4 cpd, which is geometrically equivalent to 20/250 grating visual acuity. Stimulation thresholds much lower than the safety limits indicate that pixel size can be decreased further, thereby supporting even higher spatial resolution.

As opposed to acuity measurements in clinical trials, which revealed large variability between patients[11], our results were highly consistent between animals: all the rats responding to full field stimulation also responded to gratings with a 100 μm stripe width. Further behavioral experiments with animals will nonetheless be needed to verify whether electrophysiological measurements of prosthetic visual acuity correspond to behavioral and perceptual measures as well as they do with conventional visual stimulation[25,27,30]. Ultimately, visual acuity and other aspects of prosthetic visual function in human subjects will be established by careful psychophysical examination.

Methods

Implant fabrication

Photovoltaic arrays were manufactured on silicon-on-insulator wafers using a six-mask lithographic process, as described previously[13]. To produce anodic-first pulses of electric current, the n-doped and p-doped regions in the diodes were reversed, compared to the previous description. Photovoltaic arrays consisted of 70 μm pixels, separated by 5 μm trenches (Fig. 1a). Each pixel contained two or three photodiodes connected in series between the active and return electrodes arranged in a hexagonal array. A resistance between the active and return electrodes helps discharging them between the light pulses (Fig. 1c).

Infrared projection system for in-vitro recordings

For experiments in-vitro, the infrared projection system consisted of a polarization-scrambled array of NIR (880 nm) laser diodes coupled into a 400 μm multimode fiber (Dilas M1F4S22-880.3-30C-SS2.1). We collimated the laser beam at the output of the fiber, and a used a 2° divergence microlens array diffuser to improve beam homogeneity. Visible light

from a yellow (591nm) LED was coupled into the same optical path using a dichroic mirror. We used an amplitude modulation transmissive LCD screen (Holoeye HEO-0017) to form the images that were projected on the retina through the camera port of an inverted microscope (Olympus IX-71, with a 5x objective). We controlled the image on the LCD display via Matlab using the Psychophysics Toolbox v3. We controlled the timing, width and amplitude of the light pulses using a National Instruments USB-6353 data acquisition card and custom software.

We estimated visible-light receptive fields by projecting a flickering binary white noise stimulus with constant mean illumination on the photoreceptor layer of the retina[21]. The spatiotemporal monochromatic white noise stimulus consisted of 100 × 60 square pixels with each pixel 70 μm on a side, refreshed every 33.33 ms. We randomly set the relative intensity level for each pixel in each frame above or below the 0.5 mean background level at 0.5 ± 0.48. The corresponding contrast, $(I_{max} - I_{min})/(I_{max} + I_{min})$, was therefore 96%, where I_{max} and I_{min} are the maximum and minimum intensities, respectively. The light flux at the gray background level was equivalent to 22000 photons/$\mu m^2/s^1$ produced by a monochromatic source of wavelength 591 nm.

We estimated electrical receptive fields by projecting a sparse white noise stimulus on the implant, so that the stimulation order of different pixels was randomized but no more than one pixel was activated at any given time. The laser operated with 8ms pulses at 2Hz repetition rate. We chose irradiance levels of 10mW/mm^2 so that robust responses were elicited in the RGCs, without reaching saturation.

For the alternating gratings measurements, we projected square-wave linear gratings with 100% contrast using pulsed visible (10 ms) and NIR (4 ms) light, with 20 Hz flicker frequency, alternating the contrast at 1Hz. Peak NIR irradiance in these measurements was 5 mW/mm^2. We used 6 gratings phases for each stripe width (0°, 60°, 120°, 180°, 240° and 300°). We did not align the gratings with respect to the implant; therefore relative orientation of the gratings and the implant varied from preparation to preparation, but not within a single preparation. Grating stripe width and phase varied between trials and the order of the gratings presentation in each experiment was randomized.

Electrophysiological recordings in-vitro

We obtained male and female rats with retinal degeneration from a Royal College of Surgeons (RCS) colony[44] maintained at the Stanford Animal facility (P100 – 150, $n = 9$, with $n = 3$ for eRF, $n = 4$ for grating measurements and $n = 2$ for frequency characterization, no phenotype difference between male and female). We purchased female Long-Evans adult WT rats ($n = 8$, with $n = 4$ for eRF, $n = 2$ for gratings measurements and $n = 2$ for frequency characterization) from Charles River (Wilmington, MA, USA). All animals were housed in a 12-h light/12-h dark cycle with food and water ad libitum. We conducted all *in-vitro* experimental procedures in accordance with Stanford University and University of California Santa Cruz institutional guidelines and conformed to the guidelines of the Association for Research in Vision and Ophthalmology (ARVO) Statement for the Use of Animals in Ophthalmic and Vision research. We euthanized the animals (390 mg/kg pentobarbital sodium, 50 mg phenytoin sodium) before enucleating one eye. We isolated a

small piece of retina (~3 × 3 mm) and placed it between the recording array on the ganglion cell side and the photovoltaic array on the photoreceptor side (Fig. 1d, Supplementary Fig. 1). We perfused the retina with Ames solution (Sigma-Aldrich) saturated in oxygen and kept at 27°C. We sampled and recorded voltage waveforms at 20 kHz on each of the 512 electrodes of the recording array[16].

In-vitro data analysis

We initially subtracted electrical stimulation artifacts from the raw waveform traces (Supplementary Fig. 2a), which were subsequently analyzed using custom-written software[16]. We estimated electrical stimulation artifacts by averaging their shape over many (100+) trials. We subsequently aligned the average artifact shape to the raw recordings and pointwise subtracted it from them. This method often led to incomplete artifact removal during the “light on” phase of the NIR stimulus. Therefore, we blanked this phase in software in the recordings. As a consequence, we ignored all possible direct stimulation of RGCs (latency ≤ 1ms[23]) in our analysis. We performed spike detection by thresholding the artifact-removed raw traces. For the purpose of identifying action potentials of individual RGCs, all action potential waveforms underwent dimensionality reduction by principal component analysis prior to expectation-maximization clustering (Supplementary Fig. 2b). We calculated the electrophysiological images (EIs)[16] of the putative neurons by correlating voltage signals recorded over the array with the sorted spike trains (Supplementary Fig. 2c). We discarded neurons with abnormal EIs from the analysis, for example RGCs with multiple axonal tracts. We used the absence of a refractory period in the autocorrelation function exclude neuron candidates with spike trains contaminated by action potentials from other neurons.

We estimated visual receptive fields by computing the spike-triggered average (STA) RGC response to the white noise stimulus projected on the retina. We calculated the STA for each by averaging, over all spikes generated by the neuron, the sequence of stimulus frames preceding each spike[21]. The receptive field (RF) location, size, and orientation were based on the STA frame most significantly different from the mean (gray) background level. We fit this frame with a two-dimensional generalized Gaussian and we defined the RF diameter as the geometrical mean of the minor and major axes of the 1SD contour of the fitted Gaussian. This representation assumes that the STA is separable in space and time. We estimated the time filters of each neuron, which we used for functional classification by the STA time courses. We calculated these filters by averaging together the time courses of all STA pixels significantly different from the mean intensity level (a significant pixel was defined as one that differs in absolute value from the mean level by more than three times its RMS noise).

For WT retinas, we used the presence of visible RF mosaics underneath the prosthesis to check that the tissue was in healthy physiological condition throughout the recording (Supplementary Fig. 2d). We identified functional cell types following techniques previously described in the literature[40]. Briefly, we performed clustering on an array of indicators, including receptive field diameter, shape of the autocorrelation function and time

filter of the neurons to group them into functional cell types. Two mosaics found underneath the implant are shown in Supplementary Fig 2d.

For electrical stimulation, in order to detect deviations from the spontaneous firing rate that are half its standard deviation or larger with a *P* value of 0.01 and a statistical power of 0.8, a minimum of $n = 94$ trials is required[45]. We constructed peristimulus time histograms (PSTHs) by binning spikes over 5ms periods and averaged over 100 to 200 trials (Supplementary Fig. 2e–f). We defined the steady-state activity as the 300–500ms period post stimulus. For eRFs, for each 5ms time bin in the first 300ms of the signal, we compared the distribution of the spiking rate to the spontaneous spiking. If the two sets differed statistically ($P < 0.01$, two-sample Kolmogorov-Smirnov test), we considered the response as positive and defined its amplitude as the positive variation from the steady state (in number of spikes). We then constructed the eRF by encoding with gray levels the total number of action potentials elicited in the first 300ms by each pixel (Supplementary Fig. 2e). We fit the eRFs with a two-dimensional Gaussian function and used the 1SD contour to determine the eRF diameter (WT, $n = 92$ neurons across 4 preparations; RCS, $n = 48$ neurons across 3 preparations). The analysis included experimental preparations in which at least 10 RGCs underneath the implant responded to full field stimulation, with at least one action potential elicited per stimulus of 4ms in duration at 5 mW/mm^2 irradiance and 2Hz repetition rate.

Putative correlations between eRF and vRF diameters were hard to evaluate for the following reasons. Variability in the vRF diameters of cells responding both to NIR and visible-light stimulation was ± 30 μm. Photovoltaic pixels are 70 μm in size, therefore the noise introduced by the uncertainty of the cell position relative to the pixel is expected to dominate measurements of any putative correlation between eRF and vRF diameters. Additionally, we estimated vRF shapes from a 2D Gaussian fit which fails to capture the complex receptive field structure of retinal ganglion cells[46] and the Gaussian approximation introduces further noise in the measurement. Recording from a population of cells with a larger spread in vRF diameters would improve the signal-to-noise ratio of the measurement, thereby presumably allowing us to check for the presence or absence of this correlation. Unfortunately, efficiency of detecting these RGCs with smaller vRFs is low in our in-vitro preparations, which prevents us from conclusively deciding whether a correlation between eRF and vRF diameters exists.

For alternating grating measurements, we obtained the response by integrating the spikes in the 250ms following the image transition and subtracting the spikes in the 250ms before the transition. We measured these responses for different phases of the gratings and defined the amplitude of the response to a particular grating width as the maximum response across all phases. We plotted this amplitude as a function of the grating stripe width and fitted it with a bell-shaped curve (gamma distribution). For each neuron, we defined the resolution threshold as the smallest grating size eliciting more than 0.5 action potentials per contrast reversal. We performed a kernel density estimate of the threshold distribution with kernel width 4.5μm and 10μm for the visible and NIR distributions, respectively (WT, $n = 278$ neurons across 2 preparations; RCS, $n = 109$ neurons across 4 preparations). The experiments were not masked.

In-vivo implantation

For in-vivo experiments, assuming that variability between animals is similar to the measurement noise level, a minimum sample size of 4 is required to detect a VEP signal amplitude two standard deviations above the noise with a p-value of 0.05 and a statistical power of 0.8[45]. We successfully implanted 16 animals (n = 9 male Long Evans and n = 7 female and male RCS), which were all included in this study. We operated on animals at a mean age of 41 days (range 35–58 days). The subretinal implantation technique was similar to the one previously reported by our group[14]. We anaesthetized animals with a mixture of ketamine (75mg/kg) and xylazine (5mg/kg) injected intramuscularly. We made a 1.5-mm incision through the sclera and choroid 1.5mm posterior to the limbus, lifter the retina with an injection of saline solution, and inserted the implant into the subretinal space. We sutured the sclera and conjunctiva with nylon 10-0 and applied topical antibiotic (Bacitracin/ Polymyxin B) on the eye post operatively. We conducted all *in-vivo* experimental procedures in accordance with the Stanford University institutional guidelines and conformed to the guidelines of the Association for Research in Vision and Ophthalmology (ARVO) Statement for the Use of Animals in Ophthalmic and Vision research.

In-vivo imaging

We evaluated the anatomical integration of the device in the subretinal space by OCT (HRA2-Spectralis, Heidelberg Engineering, Heidelberg, Germany) using periodic examinations beginning 1 week after surgery. We performed autofluorescence imaging and fluorescein angiography using HRA2-Spectralis system (cSLO with 488 nm blue excitation and 500 nm green emission). We conducted fluorescence angiography following intraperitoneal injection of 0.2 mg/kg fluorescein sodium diluted in balanced salt solution.

Implantation of the cortical electrodes

We implanted three skull screw electrodes similarly to a previously published technique[47], and secured them in place with cyanoacrylate glue and dental acrylic. We placed two electrodes over the visual cortex, one on each hemisphere, 4mm lateral from midline, 6mm caudal to the bregma. We implanted one reference electrode 2mm right to the midline and 2 mm anterior to the bregma. Nose and tail needle electrodes served as a reference and the ground, respectively. Recordings started 2 weeks after the subretinal implantation.

Anesthesia during recordings

We anaesthetized rats with a mixture of ketamine (37.5mg/kg) and xylazine (2.5mg/kg) injected intramuscularly. We took the following steps to assure steady anesthesia: we periodically checked spontaneous eye movements and respiratory pattern, administered supplementary injections of half the initial dose every 45 minutes or as needed, and limited recording sessions to 120 minutes per session. We used a heating pad to maintain the body temperature at 37.5±0.5°C. We conducted electrophysiological recordings with a dim-room illumination of 250nW/cm^2.

Retinal stimulation in-vivo

The stimulation system (Fig. 5c) included a single-mode pigtailed NIR (915 nm) laser diode and a visible-light (532 nm) laser diode coupled into a 1 mm diameter optical fiber. The collimated output beam illuminated a Digital Micro-mirror Device (DMD, DLP Light Commander, LOGIC PD) to form the patterns. We mounted the optical system on a slit lamp (Zeiss SL–120) to allow direct observation of the patterns on the retina. Following the pupil dilation, we covered the cornea with a viscoelastic gel and a cover slip to cancel the optical power of the eye and ensure good retinal visibility. Ocular retraction was required in some cases to help align the implant with the beam. We monitored the position of the light pattern (1mm in diameter) on the retina with a charge-coupled device (CCD) camera mounted on the same slit lamp. We applied NIR stimulation with pulse durations ranging from 1 to 20ms and peak irradiances from 0.06 to 4mW/mm^2. We generated light patterns (linear gratings) with custom software and grating sizes ranged from 6 to 200 μm per stripe. We alternated these gratings (contrast reversal) at 1Hz, while pulsing the light sources at 40Hz using 4ms flashes at 4mW/mm^2 and 100nW/mm^2 for 915nm and 532nm wavelengths, respectively. We performed contrast measurements using a 40Hz carrier frequency and 1Hz alternation between irradiance levels I_{max} and I_{min}. We defined the contrast as $(I_{max}-I_{min})/(I_{max}+I_{min})$. We kept the average peak irradiance for these measurements at 2mW/mm^2.

VEP recording and analysis

We recorded VEP signals with an Espion E2 system (Diagnosys Inc, Lowell, MA) at 1kHz sampling rate using 0.5–500Hz bandpass filter, and averaged over 250 trials for each experiment. We defined cortical thresholds for the full-field stimuli (1mm in diameter) using 10ms pulses as the minimum light intensity for which the VEP amplitude in the first 100ms after pulse was above 6 times the noise level. We defined this noise level as the standard deviation of the signal during the 50ms preceding the stimulus. We measured modulation of the VEP amplitude by light intensity using 10ms pulses and normalized to the response at 1mW/mm^2. We measured modulation of the cortical response by pulse duration using a constant irradiance of 4mW/mm^2. We recorded from all animals 1 – 7 months post-implantation. The in-vivo experiments were not masked.

Visual acuity measurements

We assessed visual acuity by recording the cortical response to alternating gratings of various spatial frequencies, as described previously[25]. In experiments with WT animals stimulated by visible light, grating stripe width varied from 6 to 200 μm (n = 7). For accurate assessment of the noise level, we applied a 40 Hz notch filter to remove oscillations due to the flicker, which appear at high grating frequencies. We defined the VEP amplitude as the difference between the maximum and minimum of the cortical signal during the first 300 ms post stimulus. For infrared stimulation, grating sizes varied from 25 to 200 μm per stripe (25, 50, 100, 150, 200 μm, n = 7) with an additional measurement at 75 μm/stripe in n = 3 animals. The eVEP response was faster than the visible-light response and we measured its amplitude during the first 100 ms post stimulus. For statistical analysis we normalized the VEP amplitude for each grating size to the maximum amplitude in each animal. We defined the noise level as the normalized amplitude at the smallest grating size (6 μm for visible

light and 25 μm for NIR). We fitted the plot of the normalized VEP amplitude as a function of the stripe width with a 2nd degree polynomial function using the 50, 100, 150, 200 μm data points for visible light, and the 75, 100, 150, 200 μm data points for prosthetic stimulation. We defined the visual acuity limit as the intersection point of the fitted curve with the noise level. We calculated the uncertainties in the acuity by computing the 3×3 covariance matrix of the polynomial fitting parameters and combining this error with the noise uncertainty, assuming independence. For the polynomial fit $y(x) = p_1x^2 + p_2x + p_3$ and noise level $y(x) = p_4$, the estimator of the intersection is defined by $\hat{x} = {-p_2 \pm \sqrt{{p_2}^2 - 4p_1(p_3 - p_4)}}/{2p_1}$. Its variance can be calculated as $\sigma^2 = D\Sigma D^{\mathrm{T}}$ with $D = \left(\frac{\partial \hat{x}}{\partial p_i}\right)_{i \in [\![1,4]\!]}$ and Σ the 4×4 covariance matrix of the polynomial fit parameters and the noise level.

For comparison, we also used linear, gaussian, sigmoidal and gamma ($y(x) = axe^{-((x-x_0)/\sigma)^2}$) functions to fit the data and extrapolate visual acuity. Among those, the second order polynomial yielded the most conservative estimate of the acuity (Supplementary Fig. 7) and it matched previously reported values for electrophysiological and behavioral acuity in normally sighted pigmented rats.

To make sure that responses to the shifting gratings were not due to the change in total amount of light between the two phases of the grating, we also measured the cortical responses to full-field illumination with various steps of contrast. Animals with prosthetic stimulation had contrast sensitivity lower than 60% (Supplementary Fig. 5), while the total amount of light on the implant did not change by more than 30% during alternation of the largest gratings, and with narrower grating stripes it was much smaller. This confirms that responses to alternating gratings are not due to the difference in total luminance between the two grating phases.

Ocular safety with high power near infra-red

Stimulation thresholds (~1 mW/mm^2) exceed the maximum natural irradiance on the retina (~1 μW/mm^2) by a factor of 1000. To avoid any problems with perception of bright light by the remaining photoreceptors, we use invisible near-infrared (NIR) light within the wavelength range of 880–915 nm. We verified that such NIR illumination did not cause any response of the retina in the absence of an implant (Supplementary Fig. 6a).

Ocular safety of the NIR radiation has been described in several prior publications[12,14]. Briefly, NIR light (880 – 915 nm) is absorbed primarily by pigmented tissues, such as the retinal pigment epithelium, with a practically negligible absorption in transparent ocular tissues. According to ocular safety standards[32], for a single-pulse exposure of duration (t) and NIR wavelength (λ) the peak irradiance limit (P_{peak}) is described by the equation $P_{peak} = 6.93\times10^{-4}C_TC_Et^{-0.25}$, where $C_T = 10^{*}0.002^{(\lambda-700)}$ and $C_E = 29.3$ W/mm^2. In our case, with t=10 ms, and λ= 905 nm the maximum irradiance is 160 mW/mm^2, more than two orders of magnitude above the threshold.

The maximum average irradiance (P_{avg}) that may be delivered chronically to the retina is calculated as $P_{avg} = 6.93\times10^{-5}C_TC_E$. For λ = 905 nm the average irradiance limit is 5.2 mW/mm^2. Therefore, even the maximum settings used in this in-vivo study (Peak = 4 mW/mm^2, t = 4 ms, and repetition rate of 40 Hz, corresponding to P_{avg} = 0.64 mW/mm^2) were still one order of magnitude below the ocular safety limit. In a realistic use case the average power will be further reduced by the sparseness of the encoded visual scene (e.g. a factor of 2 for the black-and-white square grating used in this study), and by the use of additional levels of gray, below the maximum irradiance in the image).

Supplementary Material

Refer to Web version on PubMed Central for supplementary material.

Acknowledgments

We would like to thank D. Boinagrov, E.J. Chichilnisky, M.F. Marmor and S. Picaud for stimulating discussions and encouragement. We would also like to thank J. Liao for providing the VEP recording setup, S. Lee for assistance in developing surgical procedures, as well as P. Haeusser, S. Kachiguine, P. Hottowy and A. Litke for providing and supporting the multielectrode array recording setup. Funding was provided by the National Institutes of Health (grant R01-EY-018608, D.P.), the Department of Defense (grant W81XWH-15-1-0009, D.P.), NIH CTSA (award UL1 RR025744, D.P.), and the Stanford Spectrum fund (D.P). A.S. was supported by BWF CASI and Pew Charitable Trusts Scholarship in the Biomedical Sciences. K.M. was supported by an SU2P fellowship as part of an RCUK Science Bridges award. H.L. was supported by the Foundation Voir et Entendre (Paris) and Pixium Vision.

References

1. Santos A, et al. Preservation of the inner retina in retinitis pigmentosa: A morphometric analysis. Archives of Ophthalmology. 1997; 115:511–515. [PubMed: 9109761]
2. Humayun MS, et al. Morphometric analysis of the extramacular retina from postmortem eyes with retinitis pigmentosa. Invest Ophthalmol Vis Sci. 1999; 40:143–148. [PubMed: 9888437]
3. Marc RE, Jones BW, Watt CB, Strettoi E. Neural remodeling in retinal degeneration. Progress in Retinal and Eye Research. 2003; 22:607–655. [PubMed: 12892644]
4. Jones BW, Marc RE. Retinal remodeling during retinal degeneration. Experimental eye research. 2005; 81:123–137. [PubMed: 15916760]
5. Behrend MR, Ahuja AK, Humayun MS, Chow RH, Weiland JD. Resolution of the Epiretinal Prosthesis is not Limited by Electrode Size. IEEE Transactions On Neural Systems And Rehabilitation Engineering. 2011; 19:436–442. [PubMed: 21511569]
6. Humayun MS, et al. Interim results from the international trial of Second Sight's visual prosthesis. Ophthalmol. 2012; 119:779–788.
7. Zrenner E. Fighting Blindness with Microelectronics. Science Translational Medicine. 2013; 5:210–216.
8. Jensen RJ, Rizzo JF. Thresholds for activation of rabbit retinal ganglion cells with a subretinal electrode. Experimental eye research. 2006; 83:367–373. [PubMed: 16616739]
9. Zrenner E, et al. Subretinal electronic chips allow blind patients to read letters and combine them to words. Proceedings of the Royal Society B: Biological Sciences. 2011; 278:1489–1497. [PubMed: 21047851]
10. Nanduri D, et al. Frequency and Amplitude Modulation Have Different Effects on the Percepts Elicited by Retinal Stimulation. Investigative Ophthalmology & Visual Science. 2012; 53:205–214. [PubMed: 22110084]
11. Stingl K, et al. Artificial vision with wirelessly powered subretinal electronic implant alpha-IMS. Proceedings Biological sciences / The Royal Society. 2013; 280:20130077. [PubMed: 23427175]

12. Mathieson K, et al. Photovoltaic Retinal Prosthesis with High Pixel Density. Nat Photonics. 2012; 6:391–397. [PubMed: 23049619]
13. Wang L, et al. Photovoltaic retinal prosthesis: implant fabrication and performance. Journal of neural engineering. 2012; 9:046014. [PubMed: 22791690]
14. Mandel Y, et al. Cortical responses elicited by photovoltaic subretinal prostheses exhibit similarities to visually evoked potentials. Nat Commun. 2013; 4:1980. [PubMed: 23778557]
15. Lorach H, et al. Performance of photovoltaic arrays in-vivo and characteristics of prosthetic vision in animals with retinal degeneration. Vision Res. 2014
16. Litke AM, et al. What Does the Eye Tell the Brain? Development of a System for the Large-Scale Recording of Retinal Output Activity. IEEE Trans on Nuclear Science. 2004; 51:1434–1440.
17. Devries SH, Baylor DA. Mosaic Arrangement of Ganglion Cell Receptive Fields in Rabbit Retina. Journal of neurophysiology. 1997; 78:2048–2060. [PubMed: 9325372]
18. Pillow JW, et al. Spatio-temporal correlations and visual signalling in a complete neuronal population. Nature. 2008; 454:995–999. [PubMed: 18650810]
19. Dacey, DM. Origins of perception: retinal ganglion cell diversity and the creation of parallel visual pathways. In: Gazzaniga, MS., editor. The Cognitive Neurosciences. MIT Press; 2004. p. 281-301.
20. Wassle H. Parallel processing in the mammalian retina. Nat Rev Neurosci. 2004; 5:747–757. [PubMed: 15378035]
21. Chichilnisky EJ. A simple white noise analysis of neuronal light responses. Network: Comput Neural Syst. 2001; 12:199–213.
22. Fransen JW, Pangeni G, Pardue MT, McCall MA. Local signaling from a retinal prosthetic in a rodent retinitis pigmentosa model in vivo. Journal of neural engineering. 2014; 11:046012. [PubMed: 24940618]
23. Boinagrov D, Pangratz-Fuehrer S, Goetz G, Palanker D. Selectivity of Direct and Network-mediated Stimulation of the Retinal Ganglion Cells with Epi-, Sub- and Intra-Retinal Electrodes. Journal of neural engineering. 2014; 11:026008. [PubMed: 24608166]
24. Heine WF, Passaglia CL. Spatial receptive field properties of rat retinal ganglion cells. Visual Neuroscience. 2011; 28:403–417. [PubMed: 21944166]
25. Silveira LCL, Heywood CA, Cowey A. Contrast sensitivity and visual acuity of the pigmented rat determined electrophysiologically. Vision Research. 1987; 27:1719–1731. [PubMed: 3445463]
26. Harnois C, Bodis-Wollner I, Onofrj M. The effect of contrast and spatial frequency on the visual evoked potential of the hooded rat. Exp Brain Res. 1984; 57:1–8. [PubMed: 6519219]
27. Prusky GT, West PWR, Douglas RM. Behavioral assessment of visual acuity in mice and rats. Vision Research. 2000; 40:2201–2209. [PubMed: 10878281]
28. Enroth-Cugell C, Robson JG. The Contrast Sensitivity of Retinal Ganglion Cells of the Cat. J Physiol. 1966; 187:517–552. [PubMed: 16783910]
29. Petrusca D, et al. Identification and characterization of a Y-like primate retinal ganglion cell type. The Journal of neuroscience : the official journal of the Society for Neuroscience. 2007; 27:11019–11027. [PubMed: 17928443]
30. Dean P. Visual pathways and acuity in hooded rats. Behavioural brain research. 1981; 3:239–271. [PubMed: 7271990]
31. Loudin JD, Cogan SF, Mathieson K, Sher A, Palanker DV. Photodiode Circuits for Retinal Prostheses. IEEE Trans Biomed Circuits Syst. 2011; 5:468–480. [PubMed: 23852178]
32. Delori FC, Webb RH, Sliney DH. Maximum permissible exposures for ocular safety (ANSI 2000), with emphasis on ophthalmic devices. J Opt Soc Am. 2007; 24
33. Goetz GA, Mandel Y, Manivanh R, Palanker DV, Cizmar T. Holographic display system for restoration of sight to the blind. Journal of neural engineering. 2013; 10:056021. [PubMed: 24045579]
34. Martinez-Conde S, Macknik SL, Hubel DH. The role of fixational eye movements in visual perception. Nat Rev Neurosci. 2004; 5:229–240. [PubMed: 14976522]
35. Lorach H, et al. Artificial retina: the multichannel processing of the mammalian retina achieved with a neuromorphic asynchronous light acquisition device. Journal of neural engineering. 2012; 9:066004. [PubMed: 23075696]

36. Joucla S, Yvert B. Improved Focalization of Electrical Microstimulation Using Microelectrode Arrays: A Modeling Study. PloS one. 2009; 4:e4828. [PubMed: 19279677]

37. Loudin JD, et al. Optoelectronic retinal prosthesis: system design and performance. J Neural Eng. 2007; 4:S72–S84. [PubMed: 17325419]

38. Victor JD, Shapley RM, Knight BW. Nonlinear analysis of cat retinal ganglion cells in the frequency domain. Proceedings of the National Academy of Sciences. 1977; 74:3068–3072.

39. Victor JD, Shapley RM. The nonlinear pathway of Y ganglion cells in the cat retina. The Journal of General Physiology. 1979; 74:671–689. [PubMed: 231636]

40. Anishchenko A, et al. Receptive Field Mosaics of Retinal Ganglion Cells Are Established Without Visual Experience. Journal of neurophysiology. 2010; 103:1856–1864. [PubMed: 20107116]

41. Gollisch T, Meister M. Eye Smarter than Scientists Believed: Neural Computations in Circuits of the Retina. Neuron. 2010; 65:150–164. [PubMed: 20152123]

42. Demb JB, Zaghloul K, Haarsma &, Sterling P. Bipolar Cells Contribute to Nonlinear Spatial Summation in the Brisk-Transient (Y) Ganglion Cells in Mammalian Retina. J Neurosci. 2001; 21:7447–7454. [PubMed: 11567034]

43. Rossi EA, Roorda A. The relationship between visual resolution and cone spacing in the human fovea. Nat Neurosci. 2009; 13:156–157. [PubMed: 20023654]

44. Strauss O, Stumpff F, Mergler S, Wienrich M, Wiederholt M. The Royal College of Surgeons Rat: An Animal Model for Inhereted Retinal Degeneration with a Still Unknown Genetic Defect. Acta Anatomica. 1998; 162:101–111. [PubMed: 9831756]

45. Whitley E, Ball J. Statistics review 4: Sample size calculations. Crit Care. 2002; 6:335–341. [PubMed: 12225610]

46. Field GD, et al. Functional connectivity in the retina at the resolution of photoreceptors. Nature. 2010; 467:673–677. [PubMed: 20930838]

47. You Y, Klistorner A, Thie J, Graham S. Latency Delay of Visual Evoked Potential Is a Real Measurement of Demyelination in a Rat Model of Optic Neuritis. Investigative Ophthalmology & Visual Science. 2011; 52:6911–6918. [PubMed: 21791585]

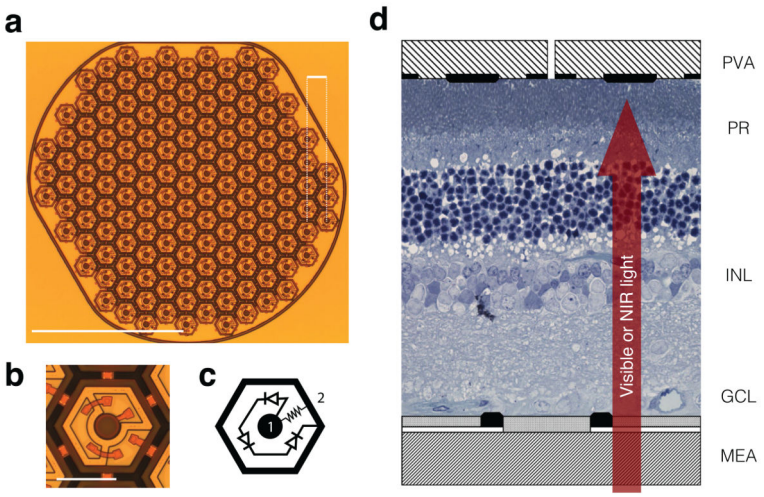

Figure 1. Photovoltaic array and in-vitro experimental setup

(**a**) The prosthesis is composed of 70 μm pixels separated by 5 μm trenches arranged in a 1 mm-wide hexagonal pattern, with the adjacent rows separated by 65 μm. Scale bar, top right-hand corner: 65 μm; bottom left-hand corner: 500 μm. (**b**, **c**) Each pixel consists of two to three (shown here) photodiodes connected in series between the central active (1) and surrounding return electrode (2). Scale bar: 50 μm. (**d**) Schematic representation of a healthy rat retina sandwiched between a transparent multielectrode array (MEA) and the photovoltaic array (PVA). Visible light stimulates the photoreceptors (PR), while much brighter pulsed NIR (880–915 nm) illumination generates biphasic pulses of current in the photovoltaic pixels, stimulating the cells in the inner nuclear layer (INL).

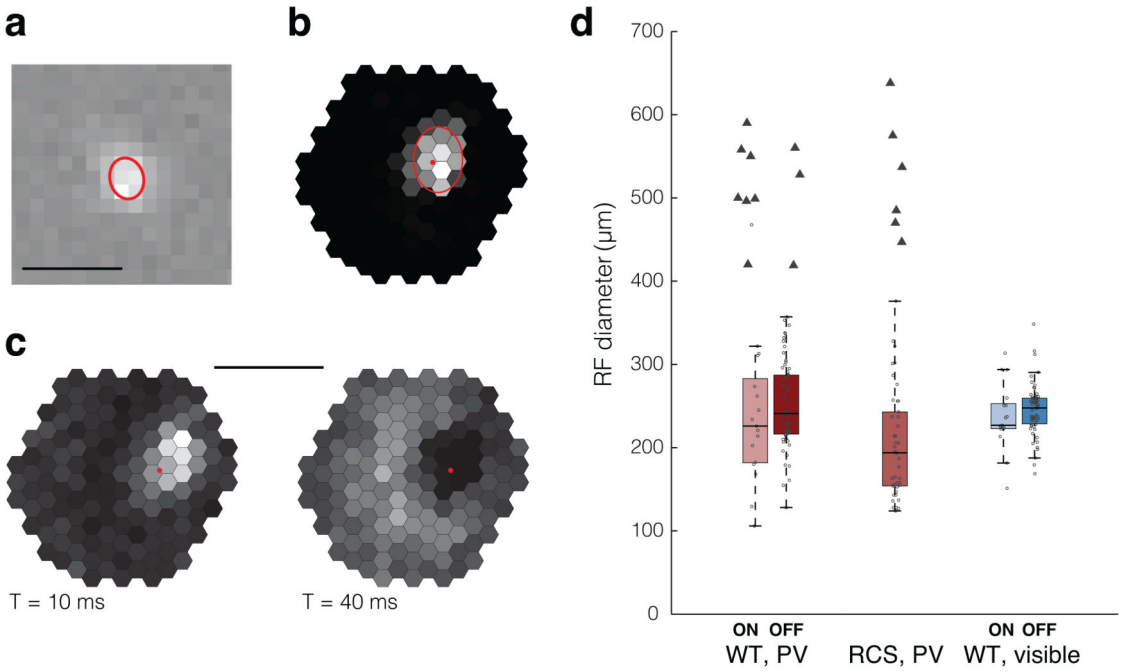

Figure 2. Natural and prosthetic receptive fields of RGCs

(**a**) Visible-light receptive field (vRF) of an ON RGC. The red ellipsoid corresponds to the 1 standard deviation (SD) contour of a Gaussian fit. Scale bar: 500 µm. (**b**) Electric receptive field (eRF) of a different RGC. Gray levels encode the number of spikes in response to stimulation of different pixels: black = 0, white = maximum (2.4 action potentials/light pulse). Estimated position of the soma is indicated by the red dot. Scale bar: 500 µm. (**c**) eRF with an earlier local and a delayed diffuse response. (**d**) Distribution of eRF (red, photovoltaic, n = 92 for WT and n = 48 RGCs for RCS animals) and vRF (blue, visible, n = 92 RGCs) diameters in healthy (WT) and degenerate (RCS) retinas. Error bars represent the standard deviation, circles correspond to localized eRFs, triangles to eRFs with a diffuse component. Box plots are Tukey boxplots.

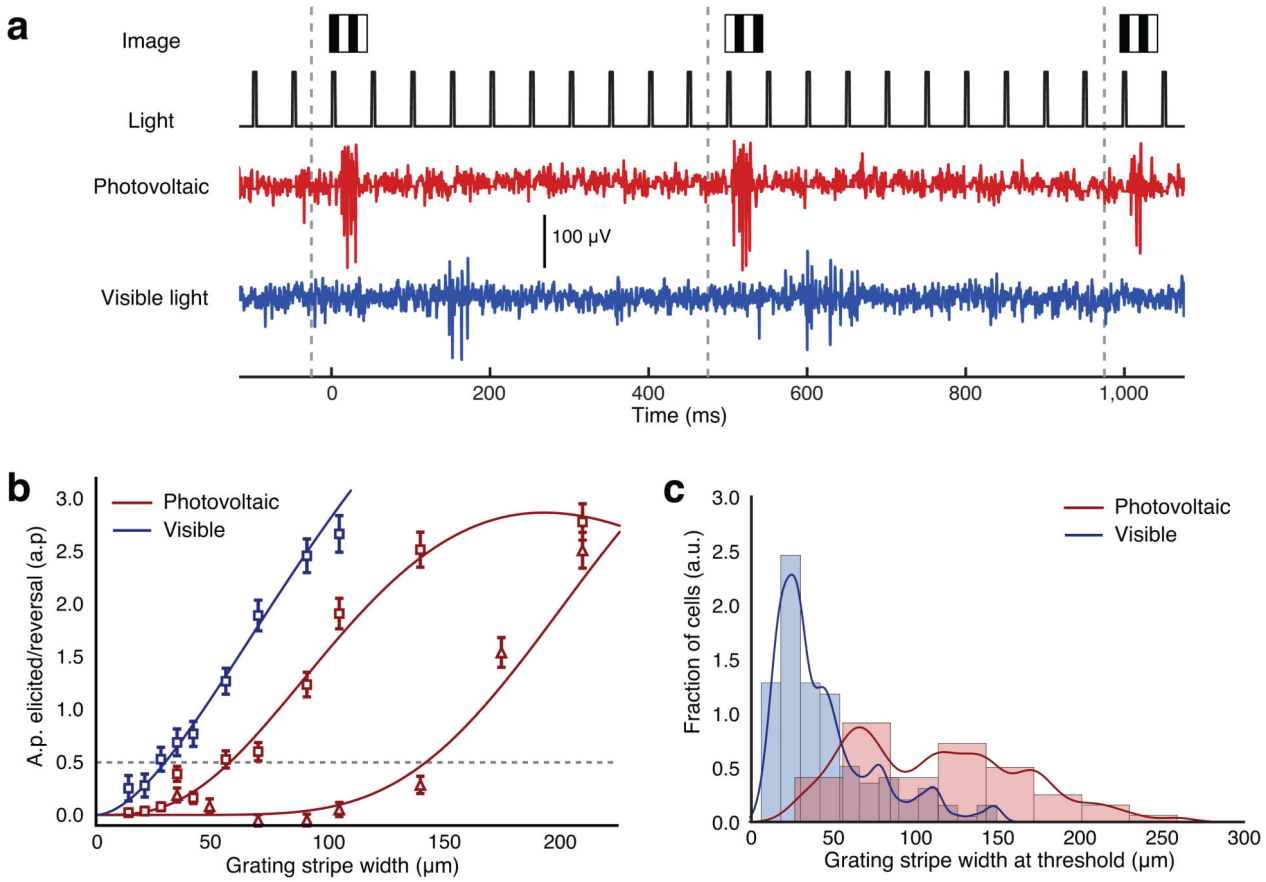

Figure 3. Response of RGCs to alternating gratings

(**a**) Light is pulsed at 20 Hz, and the grating contrast reversed at 1 Hz, corresponding to a contrast reversal every 500ms, as illustrated by the grey dashed lines. This triggers ganglion cell responses to photovoltaic (red, RCS) and visible light (blue, WT) stimulation. These RGCs do not response to individual light pulses but only to the image change at 1 Hz. (**b**) Amplitude of the response to grating reversal as a function of the grating stripe width, for one sample neuron stimulated with visible light (blue) and two sample neurons stimulated photovoltaically (red, triangles and squares). Dashes gray line indicates the stimulation threshold. Error bars show SEM. (**c**) Histograms and kernel density estimates of the stimulation thresholds distributions (0.5 spike/reversal, n = 278 RGCS for WT and n = 109 RGCs for RCS). The peak in the distribution occurs at 28 µm for visible-light stimulation. With photovoltaic stimulation, a first peak occurs at 67 µm, followed by a second peak beyond 100 µm.

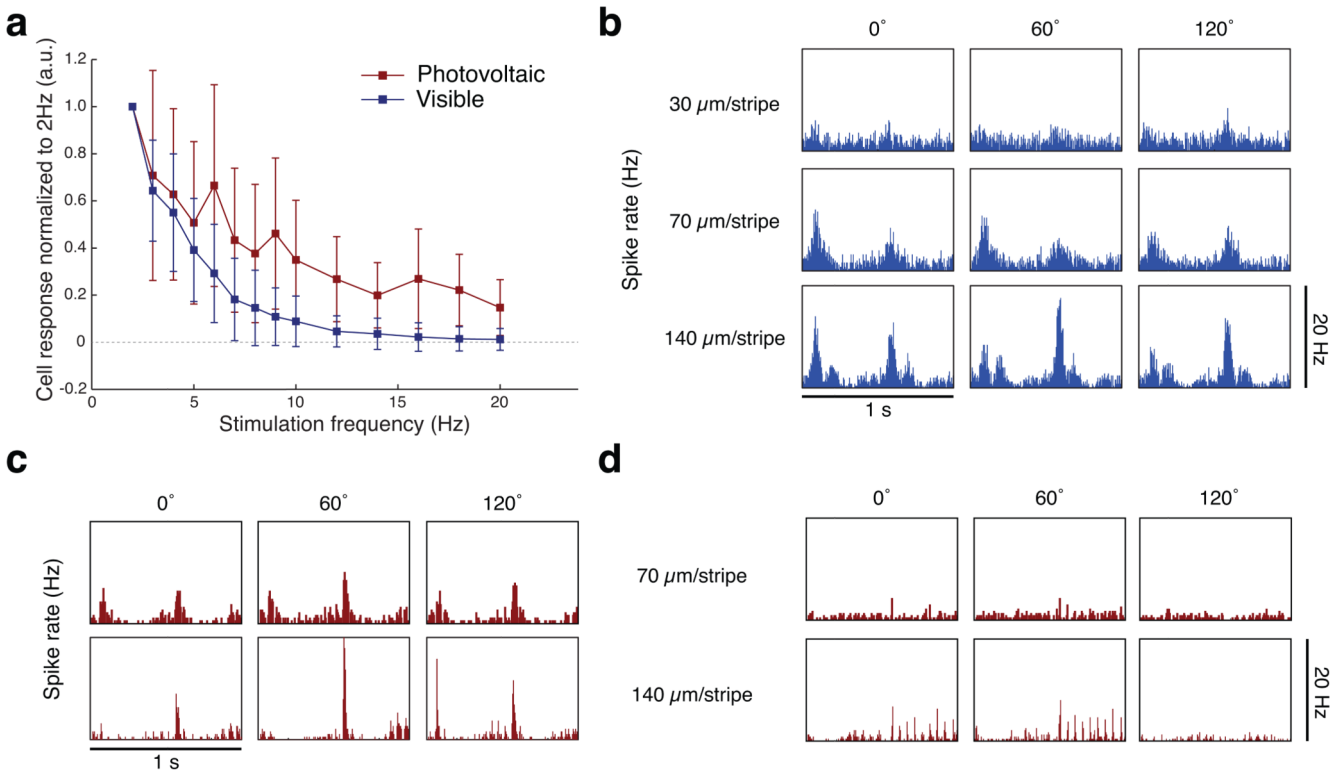

Figure 4. RGC responses to alternating gratings

(**a**) Average steady state response of RGCs to pulsed stimulation of varying frequency (*n* = 178 RGCs for WT and *n* = 45 RGCs for RCS). Amplitude of both responses decreases with increasing pulse frequency. However, while with visible-light stimulation, the steady state response at 20 Hz is negligible, a number of neurons maintain a weak response to NIR pulses at 20 Hz in the RCS retina. (**b**) RGC response to 1 Hz contrast reversal of square gratings projected with visible light onto WT retina. The response is almost imperceptible at 30 μm/stripe and exhibits a clear frequency doubling at 70 μm/stripe. At 140 μm/stripe, frequency doubling is still present, while one of the phases of the grating (60°) starts exhibiting a strong linear (f1) component. With photovoltaic stimulation of RCS retina (20 Hz, 4 ms pulses), responses vary between the RGC that exhibits strong flicker fusion, shown in (c), and RGCs that do not, as shown in (d). (**c**) In RGCs that exhibit strong flicker fusion, transient frequency-doubled response can be seen for all phases of the grating at 70 μm/stripe. At 140 μm/stripe, the frequency doubling still take place for one phase (120°), while strong linear responses can also be seen for other phases of the grating. (**d**) An RGC without flicker fusion exhibits a dominant linear response (f1) for 140 μm/stripe gratings, with action potentials time-locked to every pulse delivered to the retina. Response is negligible at 70 μm/stripe.

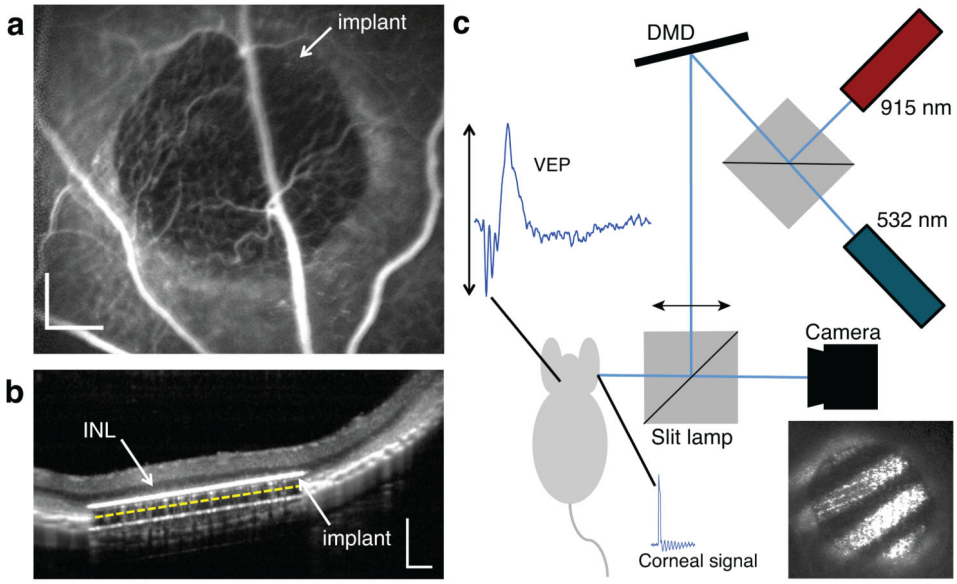

Figure 5. In-vivo subretinal implantation and stimulation setup

(**a**) Fluorescein angiography one week after surgery demonstrates normal retinal blood perfusion above the implant with no leakage. The implant is opaque to visible light and masks the choroidal fluorescence in the implanted area. Scale bar: 200 μm. (**b**) OCT shows good preservation of the inner retina, with the inner nuclear layer (INL) located approximately 20μm above the upper surface of the implant (white line). The 30 μm implant appears thicker due to its high refractive index. The yellow dashed line illustrates the actual position of the back side of the implant on top of the RPE. Scale bar: 200 μm. (**c**) Stimulation system for VEP recordings. The visible (532 nm) and NIR (915 nm) lasers illuminate the DMD which generates the spatial patterns projected onto the retina, as shown in the photograph insert. The cortical activity (VEP signal) is recorded via transcranial electrodes simultaneously to the corneal potential, which reveals the stimulation pulses from the implant.

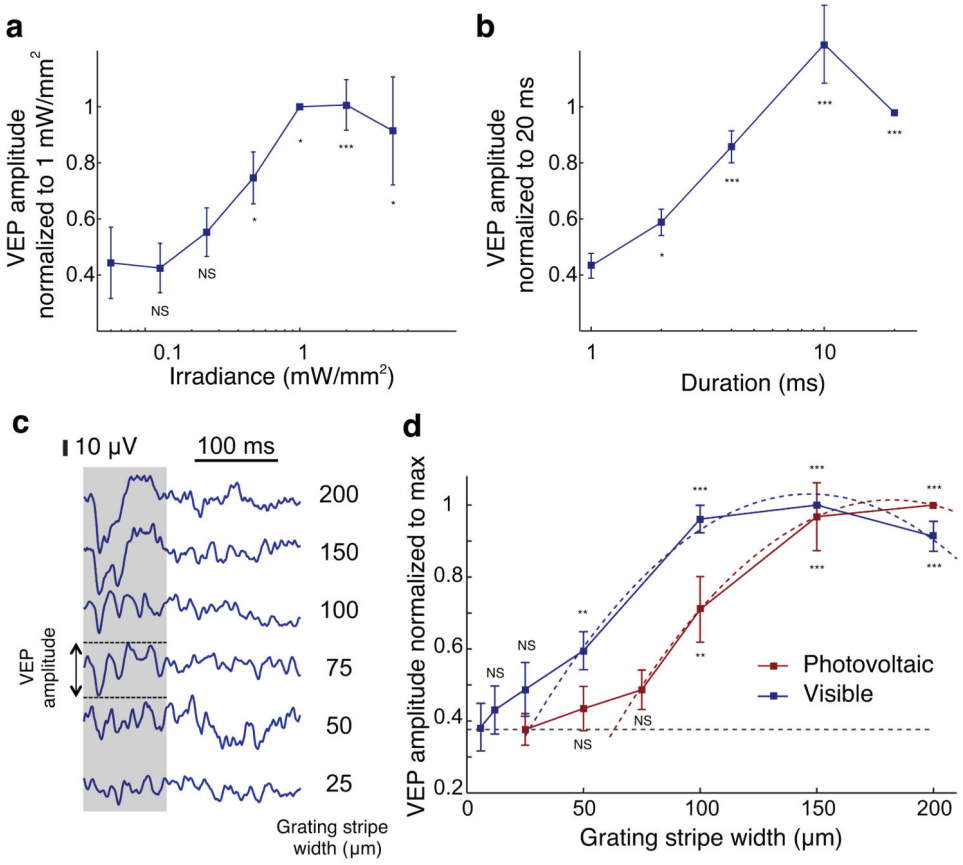

Figure 6. In vivo prosthetic stimulation and visual acuity

(**a**) VEP modulation by irradiance and (**b**) by pulse duration under full field illumination (*n* = 9 WT animals and *n* = 7 RCS animals). (**c**) Sample VEP traces corresponding to different grating stripe widths. We defined the VEP amplitude as the peak-to-peak variation of the signal during the first 100 ms following grating alternation (gray shaded area) for prosthetic stimulation. Visible light triggered slower and longer-lasting responses and we measured the amplitude during the first 300 ms after alternation. Responses decreased to the noise level with 50 µm stripes. (**d**) VEP amplitude for visible gratings (blue) and prosthetic stimulation (red) decrease with decreasing width of the stripes. Acuity limit and its associated uncertainty, estimated as the crossing point of the parabolic fits with the noise level (dashed lines), corresponds to 27 ± 9 µm/stripe for visible-light and 64 ± 11 µm/stripe for prosthetic stimulation (*n* = 7 WT animals with visible light and *n* = 7 RCS animals with prosthetic stimulation). Error bars show standard error of the mean. NS: not significant; *: $P < 0.05$; ** : $P < 0.01$: ***: $P < 0.001$, one-tailed Welch t-test.